International Journal of Engineering and Technology Innovation, vol. 14, no. 1, 2024, pp. 01-17

Simulation and Measurement Analysis of an Integrated Flow Battery Energy-Storage System with Hybrid Wind/Wave Power Generation

Li Wang[1,*], Shih-Chia Lin[1], Sheng-Jie Zhang[1], Ching-Chung Tseng[1], Hung-Hsien Ku[2], Chin-Lung Hsieh[2]

[1]Department of Electrical Engineering, National Cheng Kung University, Tainan, Taiwan, ROC

[2]Chemistry Division, Institute of Nuclear Energy Research, Atomic Energy Council, Executive Yuan,
Taoyuan, Taiwan, ROC

Received 27 April 2023; received in revised form 26 July 2023; accepted 30 July 2023

DOI: https://doi.org/10.46604/ijeti.2023.12033

Abstract

This study aims to evaluate the power-system stability and the mitigation of fluctuations in a hybrid wind/wave power-generation system (HWWPGS) under different operating and disturbance conditions. This evaluation is performed by employing a vanadium redox flow battery-based energy storage system (VRFB-ESS) as proposed. The measurement results obtained from a laboratory-scale HWWPGS platform integrated with the VRFB-ESS, operating under specific conditions, are used to develop the laboratory-scale simulation model. The capacity rating of this laboratory-scale simulation model is then enlarged to develop an MW-scale power-system model of the HWWPGS. Both operating characteristics and power-system stability of the MW-scale HWWPGS power system model are evaluated through frequency-domain analysis (based on eigenvalue) and time-domain analysis (based on nonlinear-model simulations) under various operating conditions and disturbance conditions. The simulation results demonstrate that the fluctuations and stability of the studied HWWPGS under different operating and disturbance conditions can be effectively smoothed and stabilized by the proposed VRFB-ESS.

Keywords: vanadium redox flow battery, energy-storage system, hybrid wind/wave power-generation system, laboratory-scale platform, power-system model

1. Introduction

Recently, offshore wind energy has become one of the most important renewable energy sources (RESs) to generate large electric power in European countries since such large electric power can be effectively generated from available offshore wind energy around the North Sea. With similar ocean space and electrical infrastructure, a hybrid wind/wave system also develops a novel strategy to harvest and capture energy from available RESs.

Rahman et al. [1] proposed a novel wind/wave hybrid ocean energy technology (HOET) connected to an offshore substation but without considering any ESS. This paper refers to the configuration of [1] to employ the VRFB-ESS to achieve both stability improvement and smooth fluctuations of the studied HWWPGS.

Rasool et al. [2] presented a wind/wave hybrid energy system (WWHES) using multiple permanent magnet linear generators and a doubly-fed induction generator (DFIG) for the wave and wind energy conversion system, respectively. This paper refers to the configuration of [2] to establish the HWWPGS joined with the VRFB-ESS to capture wind energy and wave energy.

---

[*] Corresponding author. E-mail address: liwangncku@gmail.com

English language proofreader: Yen-Chun Hsieh

Rasool et al. [3] proposed a novel hybrid offshore wind/wave energy conversion system (HOW-WECS) to supply stable power to the customers of remote communities. This paper refers to the configuration of [3] to establish the HWWPGS with the VRFB-ESS to achieve stability improvement.

Rasool et al. [4] showed a HOW-WECS with novel active power and reactive power control architecture using a DFIG and a linear generator to effectively capture wind energy and wave energy, respectively. This paper refers to the configuration of [4] to establish the HWWPGS for effectively harvesting wind energy and wave energy.

Gao et al. [5] presented a comprehensive review of the electrical systems to implement wind/wave energy conversion systems. This paper also refers to the configuration of [5] to establish the HWWPGS for effectively integrating wind energy and wave energy.

Latif et al. [6] proposed a novel double-stage controller for load frequency control to evaluate the dynamics in an independent hybrid maritime microgrid (MG). This paper refers to the control system of [6] by using the proposed VRFB-ESS to achieve power-flow control of the studied HWWPGS.

Jahangir et al. [7] compared both techno-economic and environmental analyses between a hybrid PV/WT/Pelamis/battery system and a hybrid PV/WT/battery system at seven different locations in the world to confirm that the former was able to yield more economic efficiency than the latter. This paper refers to the configuration of [7] to establish the studied HWWPGS joined with the proposed VRFB-ESS.

Sattar et al. [8] presented both dynamic and transient characteristics of a battery energy storage system (BESS) connected to the output terminals of a wind energy conversion system to smoothen short-term output-power fluctuations. This paper refers to the BESS in [8] to study VRFB-ESS on both smooth fluctuations and stability improvement of the HWWPGS.

Rasool et al. [9] proposed a novel multifilter-based dynamic power-sharing control devised for a hybrid energy-storage system (HESS) integrated with a WECS. This paper refers to the control system and the HESS in [9] and uses the proposed VRFB-ESS with a suitable control system to achieve both smooth fluctuations and stability improvement of the HWWPGS.

Huang and Mu [10] proposed an improved interdigital flow field design to improve the overall performance of a VRFB-ESS connected to MGs to effectively conquer the problems of randomness, intermittentness, and uncontrollability at the output powers of wind energy, PV energy, and other RESs. This paper refers to the VRFB-ESS in [10] to achieve both smooth fluctuations and stability improvement for the studied HWWPGS.

Wang et al. [11] proposed a VRFB-ESS connected to the output terminals of a wind farm through a bidirectional AC/DC converter with its control strategy to improve the power quality and stability of the wind farm. This paper refers to the configuration of [11] for establishing the studied HWWPGS.

Ma et al. [12] proposed a control scheme using a shared BESS to undertake the obligations of primary frequency response for multiple wind and PV power plants to provide commercial automatic generation control services. This paper refers to the configuration of [12] by establishing the HWWPGS joined with the proposed VRFB-ESS for power-flow control.

Wang et al. [13] presented the configuration of a WT system integrated with a VRFB-ESS supplying DC loads. The step-changed power absorbed by the DC load and the random output active power of the WTS were simultaneously compensated by the output power of the proposed VRFB-ESS. This paper refers to the configuration of [13] to establish the HWWPGS joined with the proposed VRFB-ESS to smoothen power fluctuations.

Wang et al. [14] presented comparative experimental measured results and computer-simulated outcomes of a VRFB-ESS under different charging and discharging conditions. This paper refers to the equivalent-circuit model of the VRFB-ESS in [14] and combines the models of both HWWPGS and VRFB-ESS to achieve power-system stability improvement and smooth fluctuations.

The contributions of this paper are (a) a laboratory-scale platform for power integration of a VRFB-ESS into an HWWPGS is proposed and established, (b) the measured results of the laboratory-scale platform are employed to carefully compare with the simulated ones obtained from the laboratory-scale platform's simulation model, (c) the simulation model for power integration of a VRFB-ESS into an HWWPGS is extended to be an MW-scale power-system model of the HWWPGS for evaluating power-system stability using both frequency-domain approaches based on eigenvalue analysis under different operating conditions and time-domain approach based on nonlinear-model simulations under various disturbance conditions.

The structure of this paper is organized as below. Section 2 introduces the configuration of the laboratory-scale platform and the associated employed mathematical models of the studied HWWPGS. Both field-measured steady-state results and computer simulation steady-state results of the laboratory-scale platform under the selected operating condition are compared in Section 3. Section 4 shows the frequency-domain results of the MW-scale power-system model of the HWWPGS using eigenvalues analysis. Time-domain analyzed results of the MW-scale power-system model of the HWWPGS are depicted in Section 5. Finally, important specific conclusions of this paper are drawn in Section 6.

2. Configuration of Laboratory-Scale Platform and Employed Mathematical Models

A laboratory-scale platform for power integration of a VRFB-based ESS into an HWWPGS is proposed in this paper and the associated configuration of the laboratory-scale platform is shown in Fig. 1. In Fig. 1, a three-phase permanent-magnet synchronous generator (PMSG) rated at 2 kW driven by an induction motor (IM) rated at 5.5 kW controlled by a frequency converter is employed to simulate the operational characteristics of the studied wind PGS. A three-phase linear permanent-magnet generator (LPMG) rated at 2 kW driven by a linear permanent-magnet motor (LPMM) rated at 3 kW is utilized to simulate the operational performance of the studied wave PGS. The three-phase AC outputs of the wind PMSG and the wave LPMG are rectified to be the DC-link voltage of 48 V through individual three-phase bridge rectifiers with the DC/DC converters. In addition to connecting the VRFB-ESS rated at 500 W to achieve energy-storage (charging the VRFB-ESS) or energy-release (discharging from the VRFB-ESS) functions through a bidirectional DC/DC converter, the 48-V DC link also supplies power to an AC load through a DC/AC voltage-source inverter (VSI) under various loading conditions of the HWWPGS integrated with the VRFB-ESS.

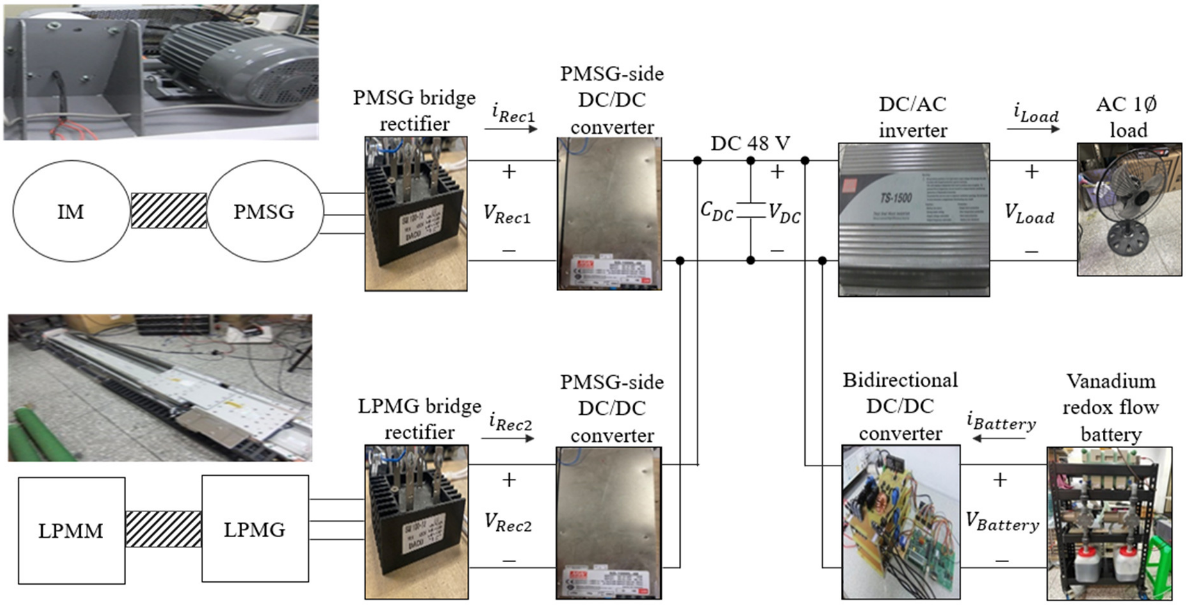

Fig. 1 Lab-scale VRFB-ESS integration in HWWPGS

The field measurement results of the laboratory-scale platform are first utilized to adjust and correct the parameters of the simulation models of the studied laboratory-scale platform. Subsequently, the capacities of the wind PGS, the wave PGS, and the VRFB-ESS are enlarged to 1 MW, 0.5 MW, and 100 kW/kWh, respectively, to establish the required MW-scale power-system model of the studied HWWPGS. The simulation results also demonstrate that the proposed MW-scale power-system model of the studied HWWPGS can operate under different scenarios, validating the feasibility and effectiveness of the HWWPGS integrated with the VRFB-ESS.

This section presents the mathematical models for various subsystems in the studied HWWPGS discussed in this paper. The model for the PMSG-based wind PGS, the model for the LPMG-based wave PGS, the model for the VRFB-ESS, and their associated control blocks for the converters/inverters are briefly discussed. All models, except for the DC components, are established in a *d-q* axis reference frame. Since only three-phase balanced conditions are considered in this paper, the zero-axis (or 0-axis) component can be properly neglected.

2.1. Model of the proposed VRFB-ESS with its bidirectional DC/DC converter [*13-14*]

The fundamental architecture of the proposed VRFB-ESS is shown in Fig. 2. It consists of a main cell stack (Labeled as “Cell Stack”), two electrolyte tanks (“Electrolyte Tank #1” and “Electrolyte Tank #2”), two circulation pumps (“Pump #1” and “Pump #2”), and two heat exchangers (“Heat Exchanger #1” and “Heat Exchanger #2” in Fig. 2). As shown in Fig. 2, “Pump #1” draws electrolyte from “Electrolyte Tank #1,” while “Pump #2” draws electrolyte from “Electrolyte Tank #2,” each corresponding to the Cathode and Anode, respectively. The reacted electrolyte flows through both “Heat Exchanger #1” and “Heat Exchanger #2,” and then returns to “Electrolyte Tank #1” and “Electrolyte Tank #2”, respectively.

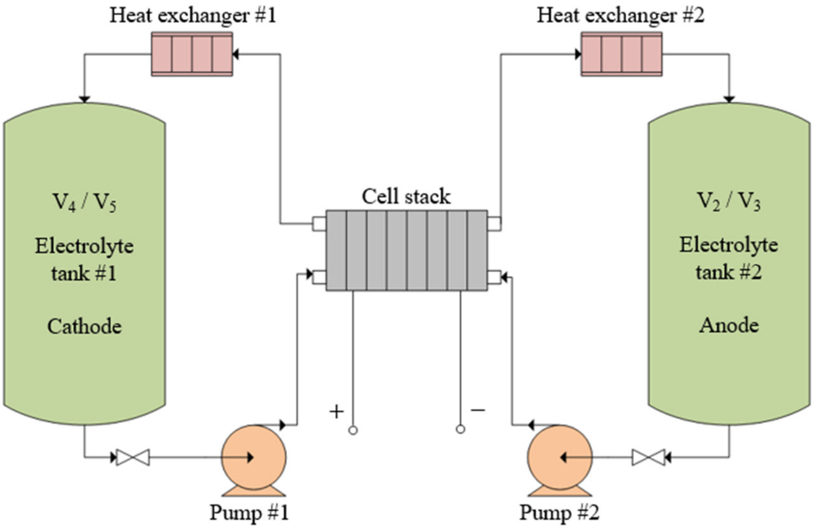

Fig. 2 Fundamental architecture of the proposed VRFB-ESS

Fig. 3 illustrates the employed equivalent-circuit model of the studied VRFB-ESS, including both equivalent internal losses and equivalent parasitic losses. In this model, V_{VRFB} and I_{VRFB} represent the output voltage and output current of the VRFB-ESS, respectively.

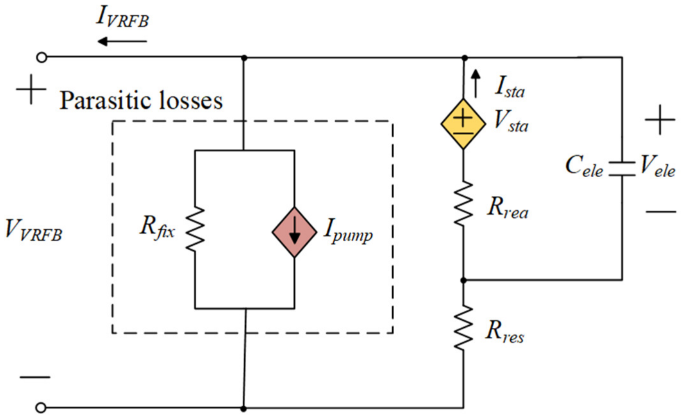

Fig. 3 Equivalent-circuit model of the employed VRFB-ESS

The parasitic loss is depicted by a parallel connection of the equivalent resistance R_{fix} (used for controller purposes) and the dependent current source I_{pump} (utilized for the circulating pumps). The dependent voltage source V_{sta}, along with its output current I_{sta}, characterizes the equivalent voltage of the cell stack. Additionally, C_{elec} denotes the equivalent capacitance of the electrode, R_{rea} is employed to represent equivalent reaction loss, and R_{res} represents an equivalent resistive loss. The VRFB-ESS cell voltage can be expressed by:

$$V_{cell} = E_0 + \frac{2RT}{F} \text{In} \frac{SOC}{1 - SOC} \tag{1}$$

where E_0 is the balance potential (in V) of individual cells, R is the universal gas constant (R = 8.314510 J/kmole), F is the Faraday constant (F = 96,485 C/mole), T is the temperature (K) of the electrolyte in the stack or the stake temperature, and SOC is the state of charge of the VRFB-ESS.

The bidirectional DC/DC converter used for the energy exchange between the VRFB-ESS and the DC link, as shown in Fig. 4, comprises an energy-storage inductor L_S and two power semiconductor switches S_1 and S_2, which operate complementarily. This configuration enables bidirectional power flow between the VRFB-ESS and the DC link. When the bidirectional DC/DC converter is in the buck mode of operation, S_1 acts as a switch, S_2 acts as a diode, and power flows from the DC link to the VRFB-ESS.

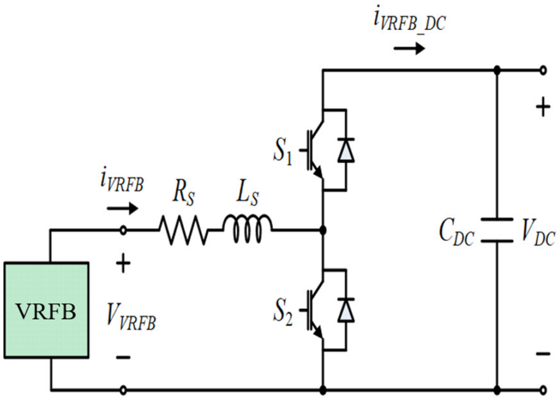

Fig. 4 DC/DC converter for VRFB-ESS energy exchange

Conversely, when the bidirectional DC/DC converter is in the boost mode of operation, S_2 acts as a switch, S_1 acts as a diode, and the power flows from the VRFB-ESS to the DC link. For simplicity, it is assumed that the detailed switching manners of two power switches, S_1 and S_2, are properly neglected. Thus, the bidirectional DC/DC converter can be simulated using its dynamic average-value model. Figs. 5(a) and 5(b) depict the dynamic average-value models of the bidirectional DC/DC converter under the boost mode of operation and the buck mode of operation, respectively.

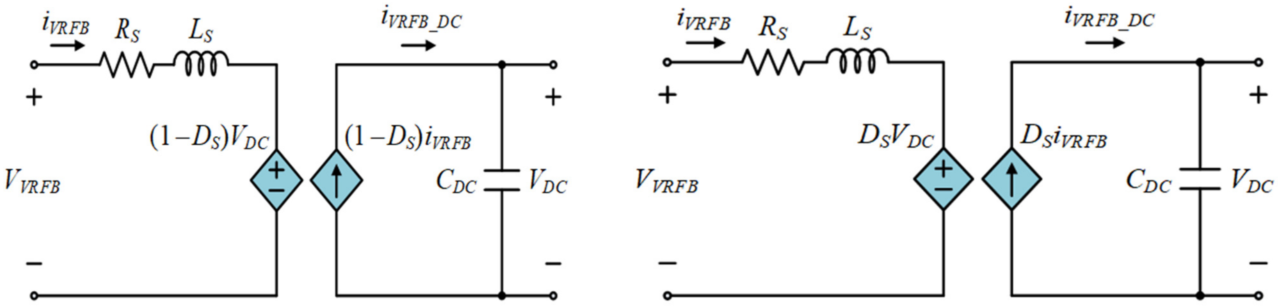

(a) Boost mode (b) Buck mode

Fig. 5 Dynamic average-value model of the employed bidirectional DC/DC converter

The associated dynamic equations of the employed bidirectional DC/DC converter in the boost mode and the buck mode of operation are given below.

(a) Boost mode:

$$(L_S)\,p(i_{VRFB}) = -R_S i_{VRFB} + V_{VRFB} - (1 - D_S)V_{DC} \tag{2}$$

$$i_{VRFB\_DC} = (1 - D_S)\,i_{VRFB} \tag{3}$$

(b) Buck mode:

$$(L_S)\,p(i_{VRFB}) = -R_S i_{VRFB} + V_{VRFB} - D_S V_{DC} \tag{4}$$

$$i_{VRFB\_DC} = D_S i_{VRFB} \tag{5}$$

where L_S and R_S are the equivalent inductance and the equivalent parasite resistance of the energy-storage inductor, respectively; i_{VRFB_DC} is current at the DC-link side; and D_S is the duty ratio of the two power semiconductor switches of the bidirectional DC/DC converter.

2.2. *Model of the PMSG-based wind PGS with its AC/DC VSC* [*15-16*]

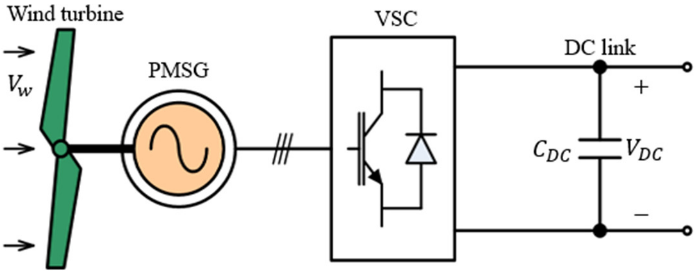

Fig. 6 Wind PMSG schematic with AC/DC VSC

Fig. 6 shows the schematic diagram of the studied PMSG-based wind PGS. The rotor of the wind PMSG is directly coupled to the WT while the stator windings of the wind PMSG are fed to the DC link through an AC/DC VSC. The mechanical power extracted by the WT can be expressed by:

$$P_w = \frac{1}{2}\rho_a \pi R_{bw}^2 V_w^3 C_{pw}(\lambda_w, \beta_w) \tag{6}$$

where ρ_a is the air density (in kg/m^3), R_t is the length of the turbine blade (in m), V_w is the wind speed (in m/s), and $C_{pw}(\lambda_w, \beta_w)$ is the dimensionless power coefficient of the WT. The power coefficient is a function of the tip speed ratio $\lambda_w = R_t\omega_t / V_w$ (where ω_t is the turbine blade's angular speed in rad/s) and the blade pitch angle β_w in degrees as follows.

$$C_{pw}(\lambda_w, \beta_w) = c_1\left[c_2/\Gamma - c_2\beta_w - c_4(\beta_w)_5^c - c_6\right]\exp(-c_7/\Gamma) \tag{7}$$

$$\frac{1}{\Gamma} = \frac{1}{\lambda_w + c_8\beta_w} + \frac{-c_9}{\beta_w^3 + 1} \tag{8}$$

where c_1-c_9 are the constant coefficients. The mathematical model of the studied wind PMSG in a *dq*-axis reference frame fixed on the rotor of the PMSG can be written as:

$$(L_{dPG}/\omega_b)\,p(i_{ds\_G}) = -R_{PG} i_{ds\_G} + \omega_{PG} L_{qPG} i_{qs\_G} - v_{ds\_G} \tag{9}$$

$$(L_{qPG}/\omega_b)\,p(i_{qs\_G}) = -R_{PG} i_{qs\_G} - \omega_{PG} L_{dPG} i_{ds\_G} - v_{qs\_G} + \omega_{PG}\psi_{PM} \tag{10}$$

where v_{ds_G} and v_{qs_G} (i_{ds_G} and i_{qs_G}) are the *d*-axis and *q*-axis stator-winding terminal voltages (stator-winding currents), respectively; L_{dPG} and L_{qPG} are the *d*-axis and *q*-axis synchronous inductances, respectively; R_{PG} is the stator-winding resistance; ψ_{PM} is the flux linkage established by a permanent magnet; ω_{PG} is the angular speed of the wind PMSG; p is the differential operator for the time variable t (i.e., $p = d/dt$); and ω_b is the base angular frequency in rad/s.

Fig. 7 depicts the control block diagram of the AC/DC VSC for the wind PMSG. The primary goal of this converter is to enable the wind PMSG to convert the maximum available wind power. To achieve this goal, the optimal torque control strategy can be employed for the wind PMSG's VSC. In this scheme, the torque of the wind PMSG is regulated to the optimum torque, which can be determined by measuring the rotor speed of the wind PMSG as follows.

$$T_{opt} = K_{opt}\omega_{PG}^2 \tag{11}$$

where K_{opt} is the constant determined by the characteristics of the WT. In Fig. 7, the torque of the wind PMSG is controlled via its q-axis stator-winding current (i_{qs_G}). To minimize the power loss in the wind PMSG, the reference value of the d-axis current is set to be zero, i.e., $i_{ds\_Gref} = 0$.

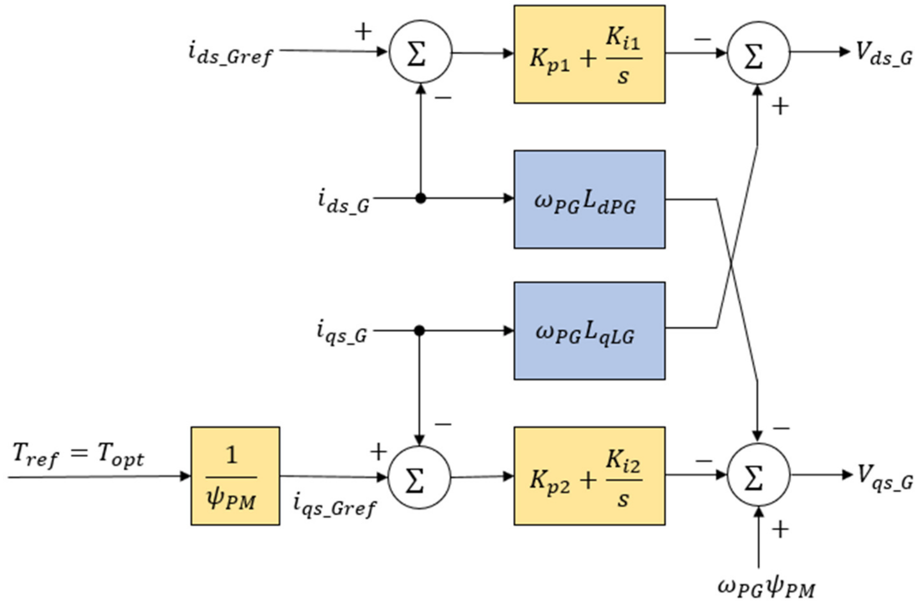

Fig. 7 Control block diagram of the employed AC/DC VSC of the wind PMSG

2.3. *Model of the LPMG-based wave PGS with its AC/DC VSC* [17]

The wave PGS consists of a LPMG driven by an AWS. The AWS is characterized as a point absorber-type wave energy converter since it is relatively small in size compared to typical wavelengths. The LPMG-based wave PGS is completely submerged, operating based on the changes in water pressure below the sea surface caused by passing waves. Fig. 8 shows the schematic diagram of the fundamental operation of the studied LPMG-based wave PGS.

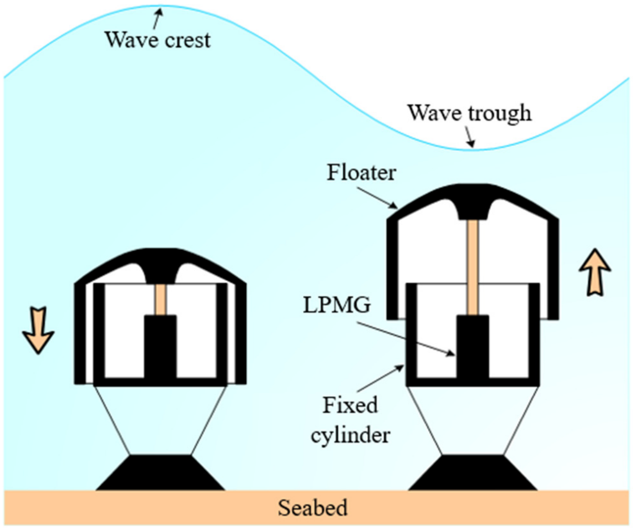

Fig. 8 Schematic diagram of the fundamental operation of an LPMG-based WAS

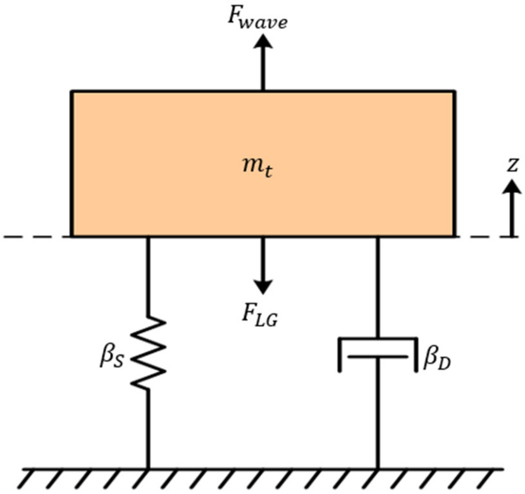

Fig. 9 Schematic diagram of the equivalent mass-spring-damper model of the studied AWS

The AWS comprises an air-filled cylindrical chamber consisting of a movable upper part, called the floater, and a lower part fixed to the seabed. The mechanical dynamics of the studied LPMG-based AWS, as shown in Fig. 9, can be modeled using a mass-spring-damper system. Thus, the mechanical dynamics of the AWS can be described by the following motion equation.

$$p(z) = u_z \tag{12}$$

$$(m_t)p(u_z) = F_{wave} - \beta_S z - \beta_D u_z - F_{LG} \tag{13}$$

where z and u_z are the distance and the speed of the floater, respectively; m_t is the total combining mass of the floater, the LPMG's translator, the water above the AWS that has to be accelerated, and various parts moving with the floater; F_{wave} is the driving force acting on the floater from the waves; F_{LG} is the force acting on the floater from the LPMG; and β_S and β_D are the spring constant and damping coefficient of the AWS, respectively.

The moving part of the wave LPMG, which is called the translator, reciprocates in the LPMG. Both the speed and direction of the translator's motion change continuously. The wave LPMG model is established based on the *dq*-axis reference frame that is fixed to the translator. The *d*-axis and *q*-axis voltage equations of the LPMG can be written by

$$v_{dLG} = -R_{LG} i_{dLG} - \omega_z \psi_{qLG} + p(\psi_{dLG}) \tag{14}$$

$$v_{qLG} = -R_{LG} i_{qLG} - \omega_z \psi_{dLG} + p(\psi_{qLG}) \tag{15}$$

where v_{dLG} and v_{qLG} are the *d*-axis and *q*-axis terminal voltages, respectively; R_{LG} is stator-winding resistance; i_{dLG} and i_{qLG} are the *d*-axis and *q*-axis stator-winding currents, respectively; Ψ_{dLG} and Ψ_{qLG} are the *d*-axis and *q*-axis stator flux linkages, respectively; and $\omega_z = \pi u_z / \tau_{pLG}$, where τ_{pLG} is the pole pitch of the LPMG. The stator flux linkages of the wave LPMG can be expressed by

$$\psi_{dLG} = -L_{dLG} i_{dLG} + \psi_{mLG} \tag{16}$$

$$\psi_{qLG} = -L_{qLG} i_{qLG} \tag{17}$$

in which

$$\psi_{mLG} = L_{mdLG} I_{mLG} \tag{18}$$

$$\psi_{dLG} = L_{lLG} + L_{mdLG} \tag{19}$$

$$\psi_{qLG} = L_{lLG} + L_{mqLG} \tag{20}$$

where ψ_{mLG} is the flux linkage produced by the permanent magnet of the wave LPMG; L_{dLG} and L_{qLG} are the d-axis and q-axis synchronous inductances, respectively; L_{lLG} is the stator-winding leakage inductance; L_{mdLG} and L_{mqLG} are the d-axis and q-axis mutual inductances, respectively; and I_{mLG} is the equivalent magnetizing current of the permanent magnet.

By substituting Eqs. (17) and (18) into Eqs. (14) and (15), the mathematical equations used to simulate the dynamic behaviors of the studied wave LPMG can be expressed as follows.

$$(L_{dLG})p(i_{dLG}) = -R_{LG}i_{dLG} + \omega_z L_{qLG}i_{qLG} - v_{dLG} \tag{21}$$

$$(L_{qLG})p(i_{qLG}) = -R_{LG}i_{qLG} - \omega_z L_{dLG}i_{dLG} - v_{qLG} + \omega_z \psi_{mLG} \tag{22}$$

Finally, the force of the wave LPMG acting on the floater can be expressed by

$$F_{LG} = \frac{3\pi}{2\tau_{pLG}}\left[\left(L_{dLG} - L_{qLG}\right)i_{dLG}i_{qLG} - \psi_{mLG}i_{qLG}\right] \tag{23}$$

Fig. 10 depicts the control block diagrams of the studied VSC for the wave LPMG. The purpose of this converter is to enable the wave PGS to extract maximum power from waves while minimizing power loss in the wave LPMG. The power loss in the wave LPMG and the active power converted from the wave can be independently controlled by the d-axis and q-axis currents (i_{dLG} and i_{qLG}) of the wave LPMG, respectively.

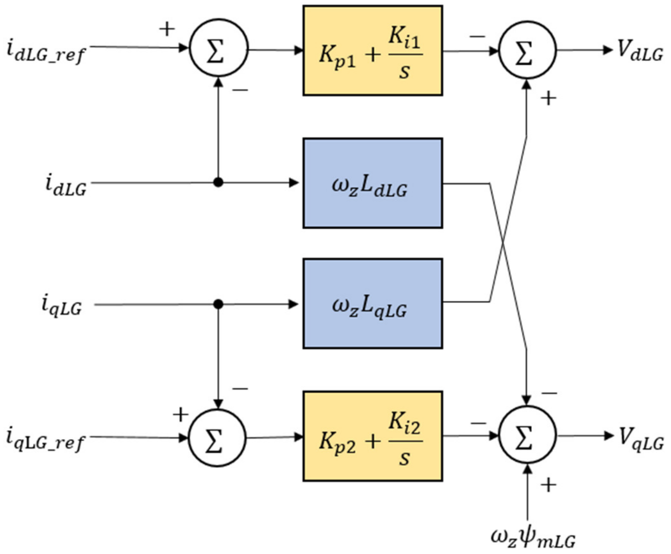

Fig. 10 Control block diagrams of the studied AC/DC VSC of the wave LPMG

The current control of the AC/DC VSC utilizes a proportional-integral (PI) controller to adjust the d-axis and q-axis currents of the wave LPMG to their reference values (i_{dLG_ref} and i_{qLG_ref}), respectively. The reference value for the d-axis current is set to zero (i.e., $i_{dLG\_ref} = 0$) to minimize power losses in the wave LPMG. To maximum power extraction from the wave, the reference value for the q-axis current is determined by the measured speed of the floater of the AWS, as shown in the following equation.

$$i_{qLG\_ref} = \frac{2\tau_{pLG}\beta_D u_z}{3\pi\psi_{mLG}} \tag{24}$$

2.4. *Model of the employed DC/AC VSI* [*15-17*]

Fig. 11 shows the control block diagram of the employed DC/AC VSI. The purpose of this DC/AC VSI is to maintain the DC-link voltage V_{DC} at its reference value V_{DC_ref} and control its output power factor at unity. Hence, the reference value i_{qI_ref} is set to zero. The DC-link voltage V_{DC} and its reference value V_{DC_ref} are measured, and the reference value for the current

i_{dI_ref} is determined through the PI controller to decouple the current components into their active and imaginary parts. The *d*-axis is aligned with the voltage phasor at the common coupling point, and the output AC voltage of the VSI can be controlled by the DC-link voltage.

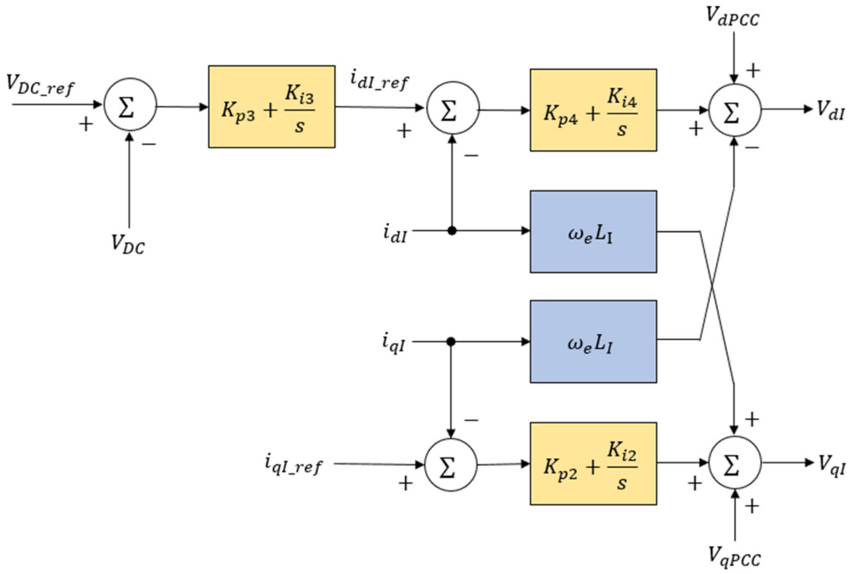

Fig. 11 Control block diagram of the employed DC/AC VSI

3. Comparative Field Measured Results and Computer Simulation Results of the Laboratory-Scale Platform

Fig. 12 shows the comparative steady-state field measured results and computer simulation results of the electrical quantities of the laboratory-scale platform for the studied HWWPGS shown in Fig. 1. The plots from Fig. 12(a) to Fig. 12(g) represent the output voltage of the wind PMSG, the output current of the wind PMSG, the output voltage of the wave LPMG, the output current of the wave LPMG, the DC-link voltage, the output voltage of the DC/AC VSI, and the voltage of the VRFB-ESS, respectively. The plots in the left column correspond to the steady-state field measured results, while those in the right column correspond to the computer simulation results.

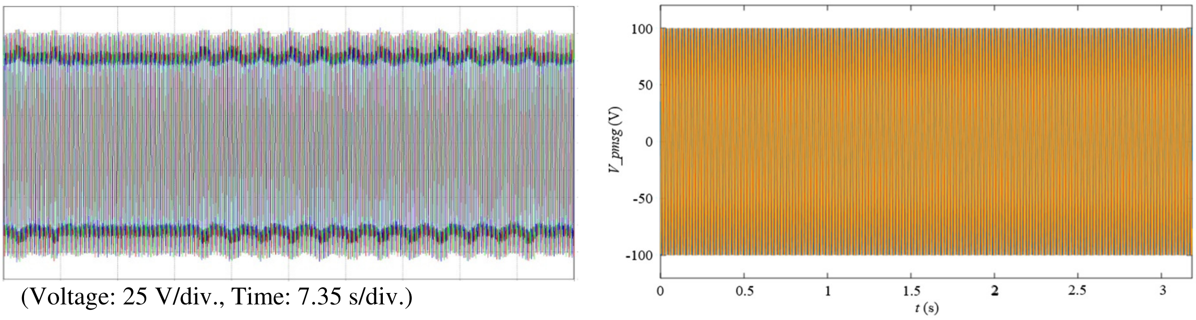

(Voltage: 25 V/div., Time: 7.35 s/div.)

(a) Output voltage of the wind PMSG

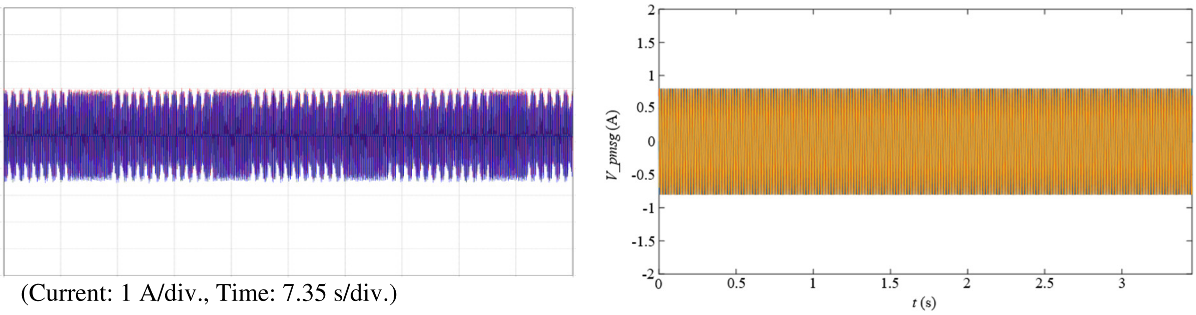

(Current: 1 A/div., Time: 7.35 s/div.)

(b) The output current of the wind PMSG

Fig. 12 Comparison: field measurements vs. simulation results for HWWPGS (Fig. 1)

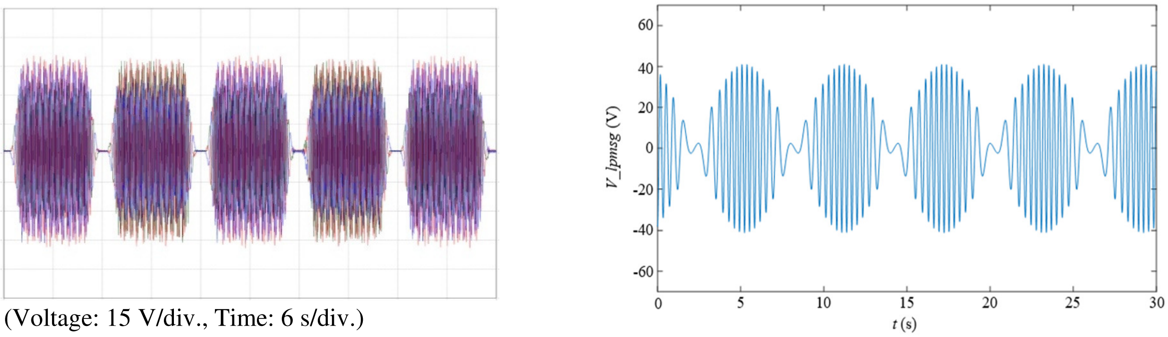

(Voltage: 15 V/div., Time: 6 s/div.)

(c) Output voltage of the wave LPMG

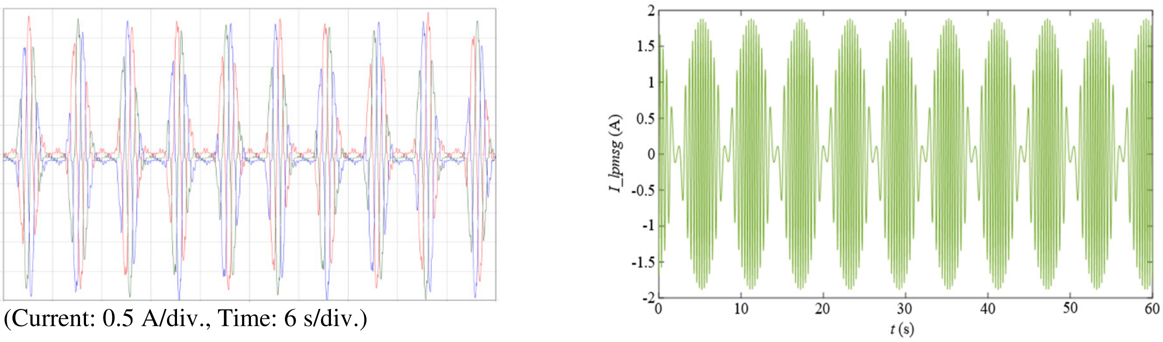

(Current: 0.5 A/div., Time: 6 s/div.)

(d) An output current of the wave LPMG

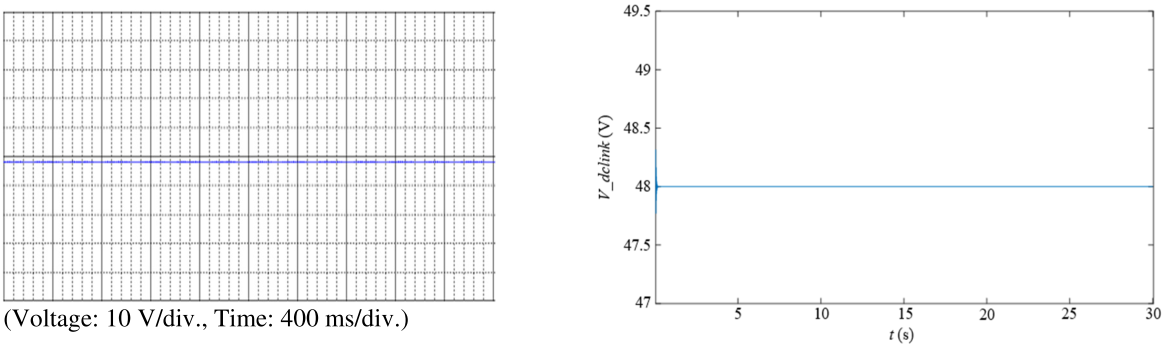

(Voltage: 10 V/div., Time: 400 ms/div.)

(e) DC-link voltage

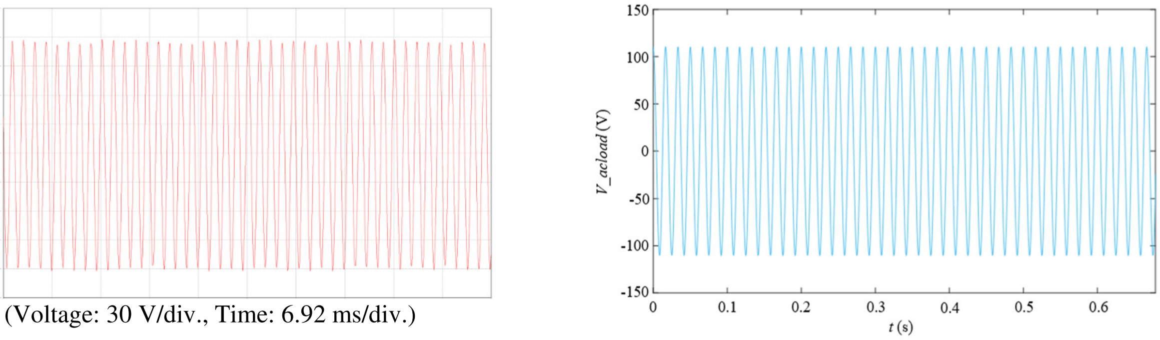

(Voltage: 30 V/div., Time: 6.92 ms/div.)

(f) Output voltage of the DC/AC VSI

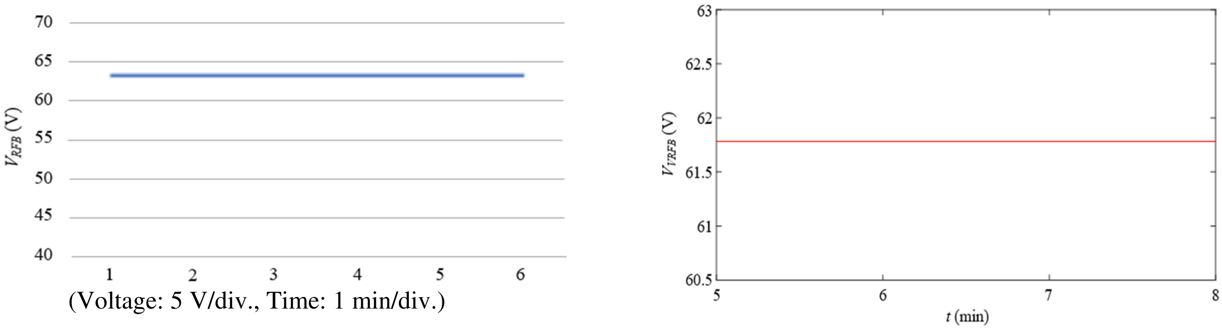

(Voltage: 5 V/div., Time: 1 min/div.)

(g) Voltage of the VRFB-ESS

Fig. 12 Comparison: field measurements vs. simulation results for HWWPGS (Fig. 1) (continued)

Table 1 provides a summary of the field-measured results and the computer simulation results for the seven electrical quantities, along with the frequency of the wind PMSG as shown in Fig. 12, as well as their corresponding errors. It can be observed from Fig. 12 and Table 1 that the current of the wave LPMG exhibits the largest error of 8.2%, while other errors remain below 4.1%. Hence, it can be concluded that the developed mathematical model for the laboratory-scale platform is suitable for establishing an MW-scale power-system model of the HWWPGS combined with the proposed VRFB-ESS in the next section.

Table 1 Comparison of field measured results, computer simulation, and error results for HWWPGS electrical quantities

	Field measured results	Computer simulations	Error (%)
V_{PMSG} (V)	101.2	100.0	1.2
I_{PMSG} (A)	0.83	0.81	3.75
f_{PMSG} (Hz)	57.1	59.5	4.03
V_{LPMG} (V)	41.8	40.2	3.98
I_{LPMG} (A)	2.11	1.95	8.2
V_{DC} (V)	47.8	48.0	1.11
V_{INV} (A)	107.8	110.0	2.0
f_{INV} (Hz)	58.9	60.0	1.83

4. Frequency-domain Analysis of the MW-Scale Power-System Model of the Studied HWWPGS [15-17]

In the previous section, the field measurement results of the laboratory-scale platform for the studied HWWPGS were used to adjust and correct the parameters of the simulation model for that configuration. However, it’s important to note that the capacity rating of the laboratory-scale platform falls within the kW range. In this section, the capacities of the wind PGS, the wave PGS, and the VRFB-ESS shown in Fig. 1 are properly enlarged to be 1 MW, 0.5 MW, and 100 kW/kWh, respectively, to establish the required MW-scale power-system model for the studied HWWPGS.

The nominal operating conditions for this MW-scale power-system model were properly selected: wind speed V_w of 11 m/s for the wind PGS, the peak wave force F_{wave} of 0.5 kN, the wave period T of 12 s for the wave PGS, and the AC load of 0.5 p.u. connected to the output terminals of the DC/AC VSI. This section will use eigenvalues and root-loci plots to evaluate the stability of the studied MW-scale power-system model of the studied HWWPGS under the nominal operating conditions and different wind speeds of the wind PGS.

Table 2 Comparison of eigenvalues in MW-scale power-system model for HWWPGS with/without VRFB-ESS

Eigenvalues without VRFB-ESS			Eigenvalues with VRFB-ESS		
$\Lambda_{1,2}$	AWS-LPMG of the wave PGS	$-33.9356 \pm j317.4194$	$\Lambda_{1,2}$	AWS-LPMG of the wave PGS	$-36.0444 \pm j316.7731$
$\Lambda_{3,4}$		$-688.5591 \pm j299.9147$	$\Lambda_{3,4}$		$-689.0253 \pm j299.7209$
$\Lambda_{5,6}$		-1337.416, -0.2265	$\Lambda_{5,6}$		-1337.417, -0.2265
$\Lambda_{9,10}$	WT and PMSG of the wind PGS	$-5.2927 \pm j14.0646$	$\Lambda_{9,10}$	WT and PMSG of the wind PGS	$-6.3437 \pm j13.5514$
$\Lambda_{11,12}$		-968.6324, -968.3104	$\Lambda_{11,12}$		-966.0377, -968.3104
$\Lambda_{13,14}$		-201.3692, -0.7989	$\Lambda_{13,14}$		-201.3926, -0.7989
$\Lambda_{15,16}$	DC/AC Inverter	$-484.3754 \pm j211.2625$	$\Lambda_{15,16}$	DC/AC Inverter	$-484.5246 \pm j210.9286$
$\Lambda_{17,18}$		$-495.8906 \pm j233.4511$	$\Lambda_{17,18}$		$-496.3371 \pm j233.2684$
Λ_{19}	DC link	-0.4515418	Λ_{19}	DC link	-1.5997138
$\Lambda_{20,21}$	AC load	$-0.5 \pm j3162.2776$	$\Lambda_{20,21}$	AC load	$-1.3184 \pm j3165.4166$
			$\Lambda_{22,23}$	VRFB-ESS	-497.0584, -204.3407
			$\Lambda_{24,25}$		-9.79784, -9.71672

Table 2 lists the comparative eigenvalues of the studied MW-scale power-system model for the studied HWWPGS with and without the proposed VRFB-ESS under nominal operating conditions. Table 2 shows that when the proposed VRFB-ESS is added to the studied system, the DC link and the load DC/DC converter modes can have larger influences while the modes of the wind PGS and wave PGS have smaller influences. Moreover, most modes of the studied system in Table 2 move away from the imaginary axis of the complex plane when the proposed VRFB-ESS is in service. Fig. 13 shows the root-loci plots of some important modes of the studied MW-scale power-system model for the studied HWWPGS when the wind speed of the wind PGS increases from 3 m/s to 15 m/s. It can be seen from Fig. 13 that only the modes of the wave PGS ($\Lambda_{1,2}$ and $\Lambda_{3,4}$) move leftward while other modes move leftward first and then move rightward when the wind speed increases. However, all the modes of the studied MW-scale power-system model of the studied HWWPGS can maintain stable operation under widely varied wind speeds.

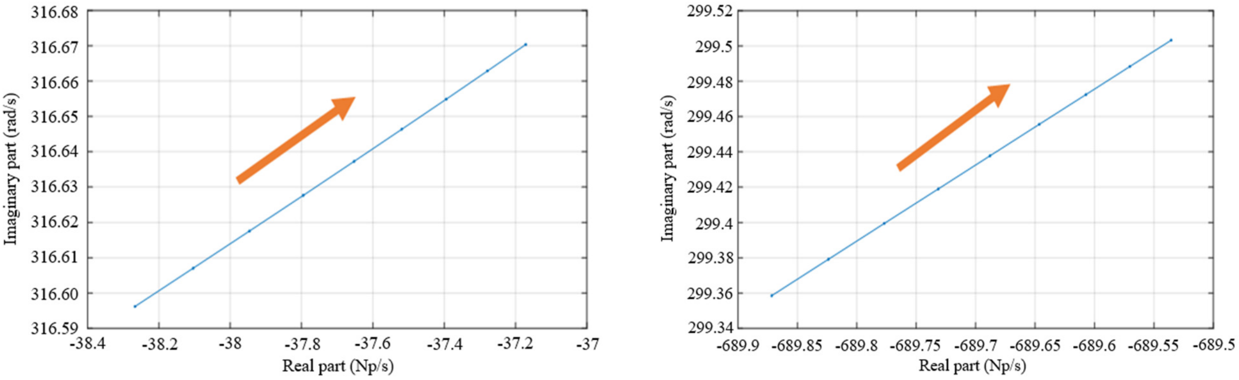

(a) Mode of the wave PGS ($\Lambda_{1,2}$) (b) Mode of the wave PGS ($\Lambda_{3,4}$)

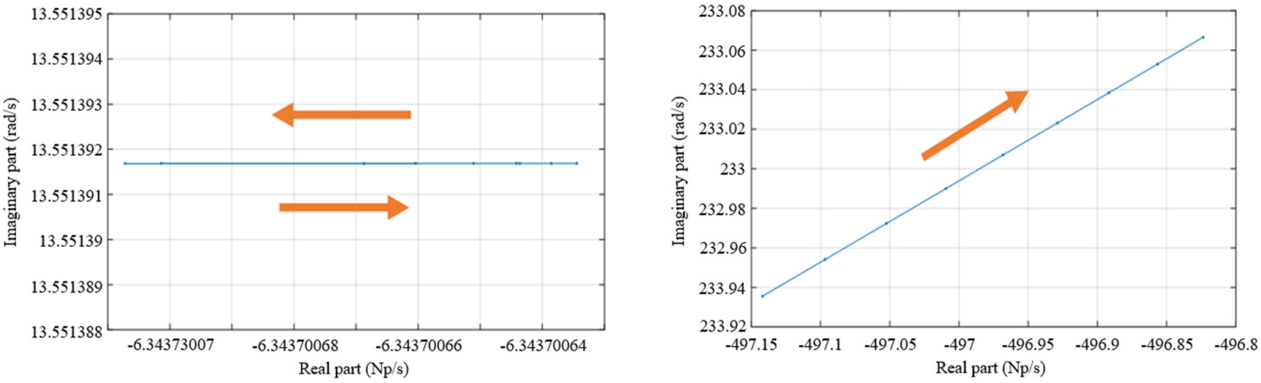

(c) Mode of the wind PGS ($\Lambda_{9,10}$) (d) Mode of the DC/AC inverter ($\Lambda_{17,18}$)

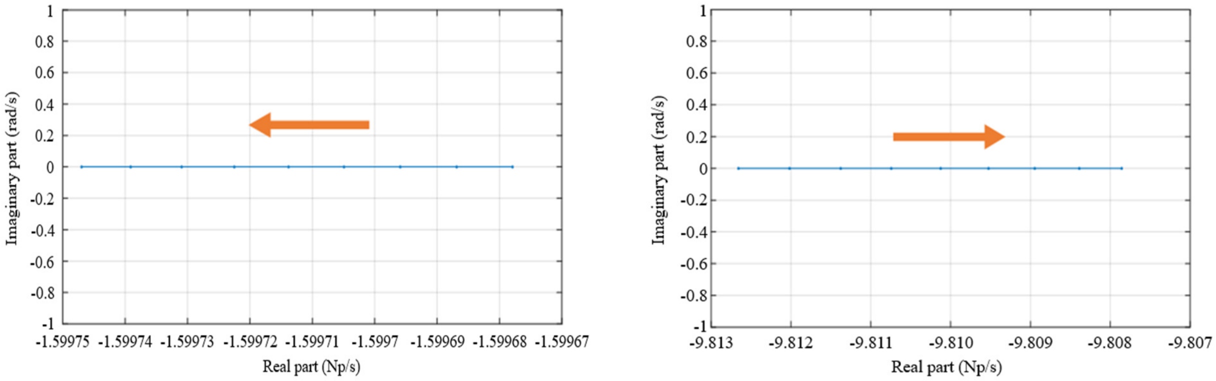

(e) Mode of the DC link (Λ_{19}) (f) Mode of the VRFB-ESS (Λ_{24})

Fig. 13 Root-loci plots for dominant modes of MW-scale power system with wind speed variation

5. Time-Domain Analysis of the MW-Scale Power-System Model of the Studied HWWPGS [15-17]

Fig. 14 shows the dynamic responses of the studied MW-scale power-system model of the studied HWWPGS when the wind speed of the wind PGS is varied. The initial conditions of the studied MW-scale power-system model of the studied HWWPGS at $t = 0$ s are the peak wave force F_{wave} of 0.5 kN and the wave period T of 12 s for the wave PGS, the absorbed power of 0.5 p.u. for the AC load, and the wind speed V_w of 11 m/s for the wind PGS. When a wind speed disturbance is applied to the studied wind PGS the wind speed gradually increases from 11 m/s to 15 m/s. When t = 15 s, the wind speed drops to as low as 10 m/s. When t = 30 s, the wind speed decreases again and then drops to 7 m/s at t = 40 s. Finally, the wind speed increases to 10 m/s.

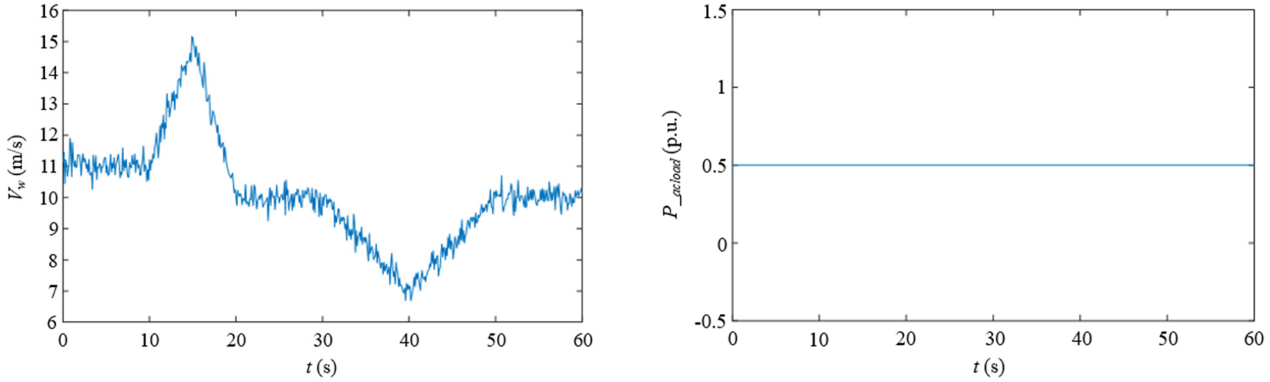

(a) Wind speed of the wind PGS (b) AC load

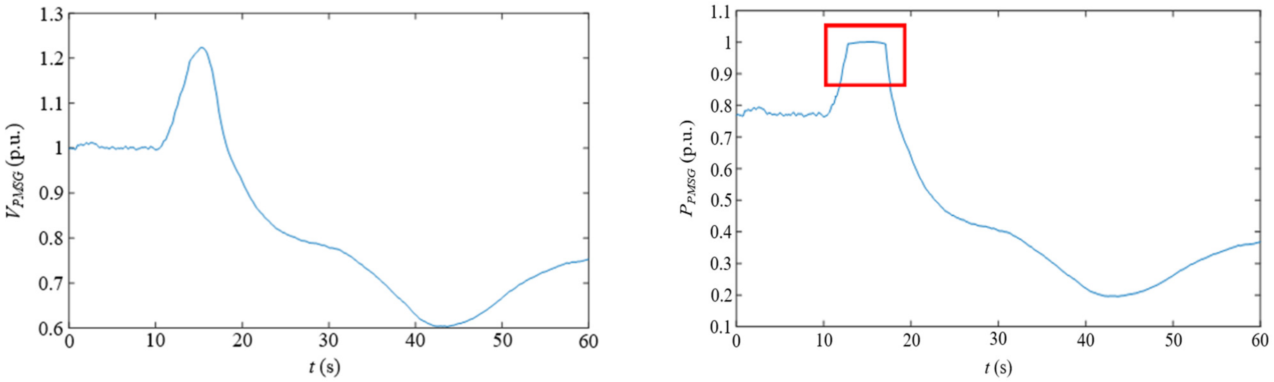

(c) The output voltage of the wind PGS (d) Output active power of the wind PGS

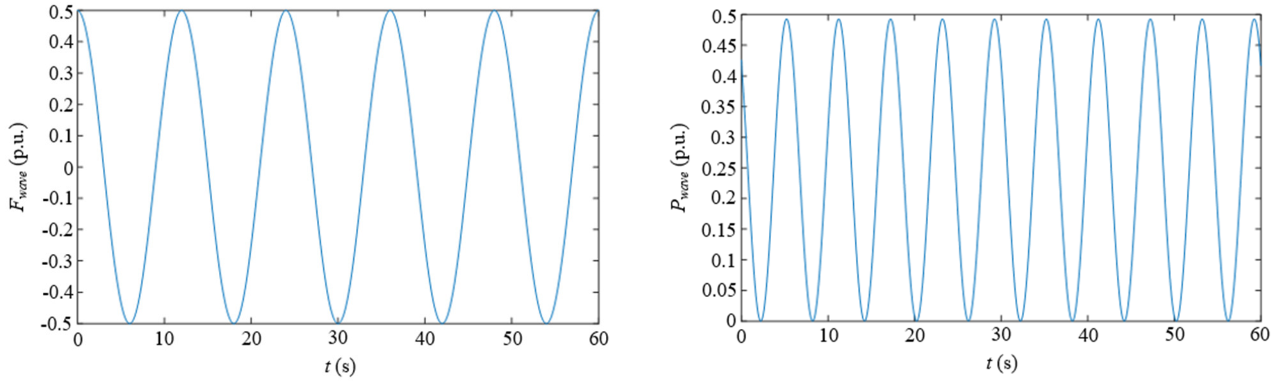

(e) Wave force of the wave PGS (f) Output active power of the wave PGS

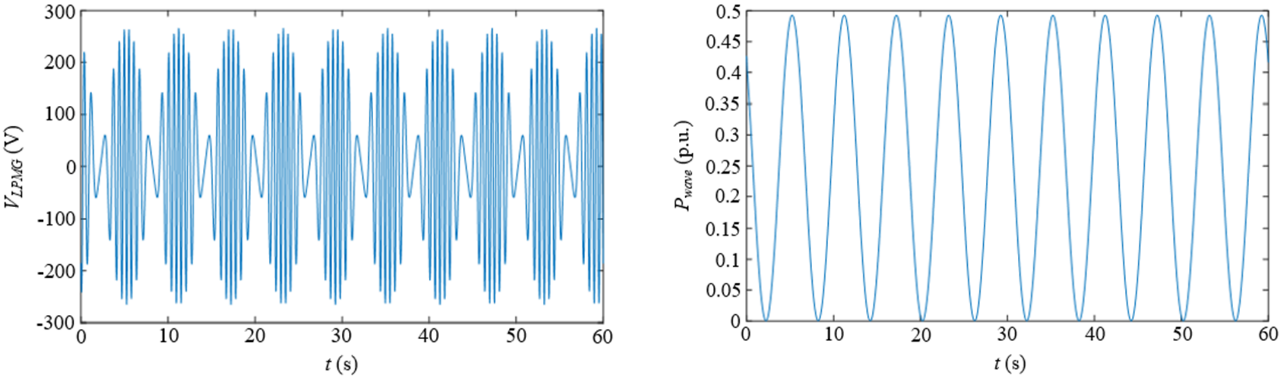

(g) Output voltage of the wave PGS (h) Floater speed of the wave PGS

Fig. 14 Dynamic responses of MW-scale power system to wind speed variations

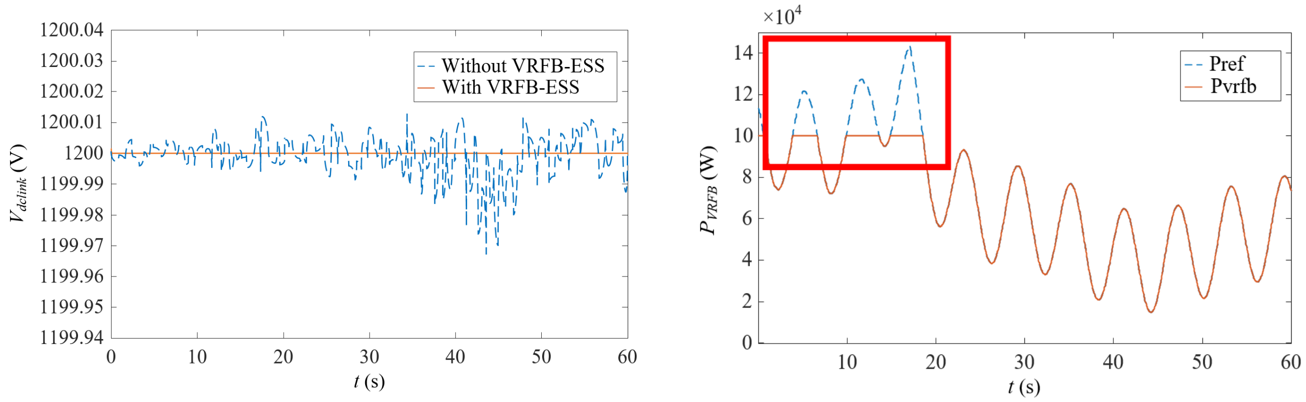

(i) DC-link voltage

(j) Reference active power and output active power of VRFB-ESS

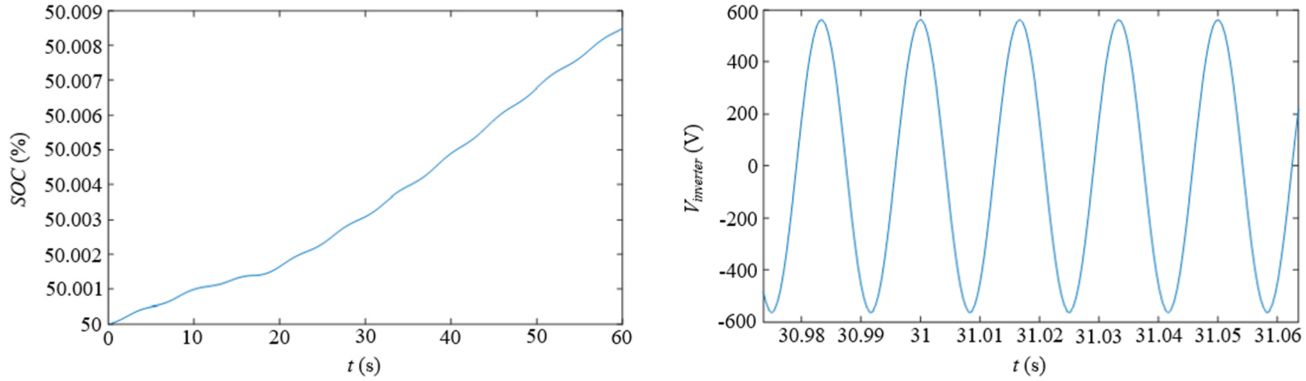

(k) *SOC* of the VRFB-ESS

(l) Output AC voltage of the DC/AC VSI

Fig. 14 Dynamic responses of MW-scale power system to wind speed variations (continued)

It can be found in Figs. 14(a)-14(d) that the voltage and the active power of the wind PGS are changed with the variations of the wind speed when the constant AC load is connected to the studied HWWPGS. It is worth noting that the output active power of the wind PGS is limited to 1.0 p.u. (as marked by a red frame) at certain time intervals as shown in Fig. 14(d). It is due to the activation of the pitch angle control system of the WT blades when the wind speed is higher than the rated wind speed of the WT.

Figs. 14(e)-14(h) shows that the output quantities of the wave PGS are not affected by the variations of the wind speed. Fig. 14(i) shows the comparative DC-link voltage of the studied MW-scale power-system model of the studied HWWPGS with and without the proposed VRFB-ESS when the wind speed of the wind PGS varies. When the proposed VRFB-ESS is not included in the studied HWWPGS, the maximum and minimum values of the DC-link voltage can be found around 1200.015 V and 1199.97 V, respectively. However, when the proposed VRFB-ESS is in service, the DC-link voltage approaches an ideal constant voltage of 1200 V regardless of wind speed changes.

Fig. 14(j) shows the dynamic responses of both reference active power and output active power of the VRFB-ESS of the studied MW-scale power-system model of the studied HWWPGS. Due to the capacity of the employed VRFB-ESS, the output active power of the VRFB-ESS cannot exactly follow the variations of the reference active power when the total surplus active power of the HWWPGS is higher than the rated capacity of the VRFB-ESS. Hence, the waveform of the reference active power shown in Fig. 14(j) is clamped to a certain level (as marked by a red frame) during some time intervals.

6. Conclusions

In this study, the laboratory-scale platform has been proposed to integrate the VRFB-ESS into the HWWPGS. The wind PGS is based on the WT-PMSG configuration with its AC/DC power converter, and the wave PGS is based on the AWS-LPMG set with its AC/DC power converter. Field-measured results of the established laboratory-scale platform for the studied

HWWPGS have been obtained for comparison with the simulation outcomes of its simulation model under a steady-state operating condition. Using the obtained simulation model, the capacity rating has been appropriately extended to create an MW-scale power-system model for the studied HWWPGS to evaluate its power-system stability. Both Frequency-domain analysis (based on eigenvalue) and time-domain analysis (based on nonlinear-model simulations) under various operating and disturbance conditions have been achieved.

The findings indicate that all the modes of the studied MW-scale HWWPGS power-system model can maintain stable operation under widely varied operating conditions. Dynamic responses of the MW-scale power-system model for the HWWPGS under varying wind speeds have also been performed. The simulation results of the MW-scale HWWPGS power-system model lead to the conclusion that the fluctuations of the HWWPGS under various operating and disturbance conditions can be effectively smoothed and stabilized by the proposed VRFB-ESS.

Conflicts of Interest

The authors declare no conflict of interest.

References

[1] M. A. Rahman, M. R. Islam, K. M. Muttaqi, and D. Sutanto, “Modeling and Design of a Multiport Magnetic Bus-Based Novel Wind-Wave Hybrid Ocean Energy Technology,” IEEE Transactions on Industry Applications, vol. 57, no. 5, pp. 5400-5410, September-October 2021.

[2] S. Rasool, K. M. Muttaqi, and D. Sutanto, “Integration of a Wind-Wave Hybrid Energy System with the Distribution Network,” IEEE International Conference on Power Electronics, Smart Grid, and Renewable Energy, pp. 1-6, January 2022.

[3] S. Rasool, K. M. Muttaqi, and D. Sutanto, “A Novel Configuration of a Hybrid Offshore Wind-Wave Energy Conversion System and Its Controls for a Remote Area Power Supply,” IEEE Transactions on Industry Applications, vol. 58, no. 6, pp. 7805-7817, November-December 2022.

[4] S. Rasool, K. M. Muttaqi, and D. Sutanto, “A Co-ordinated Real and Reactive Power Control Architecture of a Grid-Connected Hybrid Offshore Wind-Wave Energy Conversion System,” IEEE Industry Applications Society Annual Meeting, pp. 1-6, October 2022.

[5] Q. Gao, N. Ertugrul, B. Ding, and M. Negnevitsky, “Offshore Wind, Wave and Integrated Energy Conversion Systems: A Review and Future,” Australasian Universities Power Engineering Conference, pp. 1-6, November-December 2020.

[6] A. Latif, S. M. S. Hussain, D. C. Das, and T. S. Ustun, “Double Stage Controller Optimization for Load Frequency Stabilization in Hybrid Wind-Ocean Wave Energy Based Maritime Microgrid System,” Applied Energy, vol. 282, no. Part A, article no. 116171, January 2021.

[7] M. H. Jahangir, A. Shahsavari, and M. A. V. Rad, “Feasibility Study of a Zero Emission PV/Wind Turbine/Wave Energy Converter Hybrid System for Stand-Alone Power Supply: A Case Study,” Journal of Cleaner Production, vol. 262, article no. 121250, July 2020.

[8] A. Sattar, A. Al-Durra, C. Caruana, M. Debouza, and S. M. Muyeen, “Testing the Performance of Battery Energy Storage in a Wind Energy Conversion System,” IEEE Transactions on Industry Applications, vol. 56, no. 3, pp. 3196-3206, May-June 2020.

[9] S. Rasool, K. M. Muttaqi, and D. Sutanto, “A Multi-Filter Based Dynamic Power Sharing Control for a Hybrid Energy Storage System Integrated to a Wave Energy Converter for Output Power Smoothing,” IEEE Transactions on Sustainable Energy, vol. 13, no. 3, pp. 1693-1706, July 2022.

[10] Z. Huang and A. Mu, “Research on Performance Improvement Methods of Vanadium Redox Flow Battery in Microgrid,” 1st China International Youth Conference on Electrical Engineering, pp. 1-6, November 2020.

[11] W. Wang, B. Ge, D. Bi, and D. Sun, “Grid-Connected Wind Farm Power Control Using VRB-Based Energy Storage System,” IEEE Energy Conversion Congress and Exposition, pp. 3772-3777, September 2010.

[12] Y. Ma, Z. Hu, and Y. Song, “Hour-Ahead Optimization Strategy for Shared Energy Storage of Renewable Energy Power Stations to Provide Frequency Regulation Service,” IEEE Transactions on Sustainable Energy, vol. 13, no. 4, pp. 2331-2342, October 2022.

[13] L. Wang, Z. H. Huang, J. T. Lai, S. C. Lin, H. H. Ku, and C. L. Hsieh, “A Flow Battery-Based Energy-Storage System Integrated into a Wind Power-Generation System,” IET International Conference on Engineering Technologies and Applications, pp. 1-2, October 2022.

[14] L. Wang, Z. H. Huang, C. W. Tseng, M. F. Lee, C. C. Tseng, H. H. Ku, et al., “Operating Characteristics of a Vanadium Redox Flow Battery-Based Energy-Storage System,” IEEE Industry Applications Society Annual Meeting, pp. 1-8, October 2022.

[15] L. Wang, C. Y. Lin, H. Y. Wu, and A. V. Prokhorov, “Stability Analysis of a Microgrid System with a Hybrid Offshore Wind and Ocean Energy Farm Fed to a Power Grid Through an HVDC Link,” IEEE Transactions on Industry Applications, vol. 54, no. 3, pp. 2012-2022, May-June 2018.

[16] L. Wang, Q. S. Vo, and A. V. Prokhorov, “Stability Improvement of a Multimachine Power System Connected with a Large-Scale Hybrid Wind-Photovoltaic Farm Using a Supercapacitor,” IEEE Transactions on Industry Applications, vol. 54, no. 1, pp. 50-60, January-February 2018.

[17] L. Wang, Q. S. Vo, and A. V. Prokhorov, “Dynamic Stability Analysis of a Hybrid Wave and Photovoltaic Power Generation System Integrated into a Distribution Power Grid,” IEEE Transactions on Sustainable Energy, vol. 8, no. 1, pp. 404-413, January 2017.